Nano Research

Open Access

Research Article

Hydrogen-bonded organic framework-ionic liquid composite quasi-solid electrolyte for high-performance lithium battery

Junmei Zhang, Yatao Wu, Chenye Wang, Yong Liu ✉, Zhirong Yang, Shiyue Zhou, Wenpeng Li, Wenjia Wu ✉, and Jingtao Wang

School of Chemical Engineering, Zhengzhou University, Zhengzhou 450001, China

Cite this article: *Nano Research*, **2025**, *18*, 94906993. https://doi.org/10.26599/NR.2025.94906993

ABSTRACT: Ionic liquids (ILs) hold great promise as high-performance electrolyte material due to their unique advantages including nonvolatility, high thermal stability and high ionic conductivity. However, the IL-based electrolytes always suffer from serious ion aggregation and high viscosity at low temperatures, leading to significantly decline in ionic conductivity. Here, hydrogen-bonded organic framework-ionic liquid composite quasi-solid electrolyte (high temperature treatment (HT)-HOF-IL CQSE) was prepared through confining the IL electrolytes (ILEs) into the pore of HOF lamellar framework. The weak hydrogen bonding interactions within HOF nanosheets, together with the generated interactions between ILE and HOF, enable uniform and continuous distribution of ILE in HOF lamellar framework. This effectively inhibits the ion migration of ILE, which meanwhile serves as Li^+ transfer sites, affording high ionic conductivity of 5.7×10^{-5} S·cm^{-1} at −60 °C, with high lithium-ion transference number of 0.69, whereas ILEs usually lose ionic conduction ability at such low temperatures. The assembled Li symmetrical cell can stably cycle at 0.2 mA·cm^{-2} and −20 °C for more than 1500 h. The $LiFePO_4$|HT-HOF-IL CQSE|Li cell shows excellent cycling performance at 0.5 C at a wide temperature range of −20 to 60 °C. This work may pave a new avenue for the development of high-performance IL-based composite electrolytes.

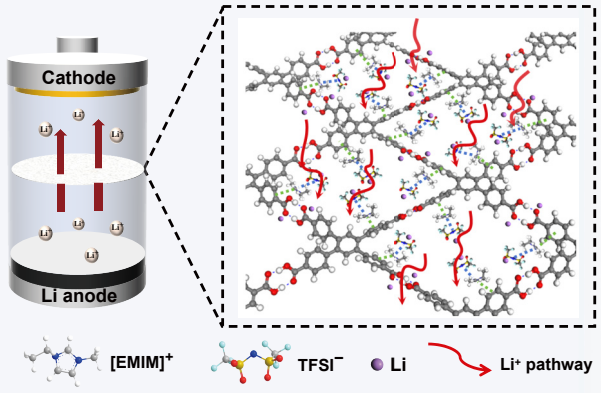

KEYWORDS: ionic liquid, hydrogen-bonded organic framework, low-temperature ionic conductivity, lithium-ion transference number, quasi-solid electrolyte

1 Introduction

Although traditional carbonate-based electrolytes have been extensively used in lithium batteries due to the high ionic conductivity, their volatility and flammability bring serious safety risk [1–4]. Compared with carbonate-based electrolytes, ionic liquid-based electrolytes (ILEs) possess unique advantages related to safety issues, such as nonvolatile, nonflammable and wide electrochemical window [5–7]. Meanwhile, ILEs also display acceptable ionic conduction property at and above room temperature [8–10]. However, compared with carbonate-based electrolytes, ILEs suffer from more obvious deterioration in ionic conductivity at low temperatures (< 0 °C), due to the sharply increased viscosity and thus ion aggregation [11–14].

The ion aggregation issue of ILEs at low temperatures can be alleviated by adding low viscosity diluent [15, 16]. For example, in order to avoid the serious ion aggregation of ILEs at low temperatures and avoid the formation of complex Li^+ solvation structure, Liu et al. diluted ILEs with low-viscosity and non-solvating co-solvents to prepare locally concentrated ILEs (LCILEs). The LCILE exhibited a high ionic conductivity of 1.67×10^{-3} S·cm^{-1} at −20 °C [17]. Despite the high ionic conductivity, these liquid electrolytes generally present low Li^+ transference numbers (t_{Li^+}) due to the strong ionic nature of ILs, which will lead to serious concentration polarization and be detrimental to the long-life cycle of batteries [18–20]. Some researchers attempted to alleviate the ion aggregation and increase the t_{Li^+} of ILEs by compositing ILEs with nanoporous solid materials, such as covalent-organic frameworks (COFs) [21, 22] and metal-organic frameworks (MOFs) [23, 24]. Tian et al. reported two COF-IL composite electrolytes by incorporating ILE (N,N-diethyl-N-(2-methoxyethyl)-N-

Received: July 3, 2024; **Revised:** August 14, 2024
Accepted: August 18, 2024

✉Address correspondence to Yong Liu, yongliu@zzu.edu.cn; Wenjia Wu, wenjiawu@zzu.edu.cn

methylammoniumbis(trifluoromethylsulphonyl)imide (DEME-TFSI)-LiTFSI) into COFs through mechanical mixing. The strong interactions between COFs and mobile $TFSI^-$ anions, as well as the nanosized pores that can trap larger anions, are supposed to be the main reasons for the more effective transfer of Li^+ and the increase of t_{Li^+}. The COF-IL composite electrolyte displays a higher t_{Li^+} (0.396) than the bare DEMETFSI IL electrolyte (0.210) [22]. Wang et al. mixed the MOF with ILEs and pressed it into pellets to prepare Li-IL@MOF composite electrolyte, in which the porous MOF provides a stable framework and the ILEs serve as Li^+ conductors [24]. It was found that the MOF framework could impose steric effect on the ion migration of ILEs, thus improving the t_{Li^+} from 0.14 to 0.36. However, the conductivity of Li-IL@MOF was only 2.2×10^{-5} S·cm^{-1} at −20 °C, due to that ILEs could not form continuous distribution within the MOF framework because of the rigid pore structure, meanwhile, MOF itself cannot effectively conduct Li^+ [25]. Hence, it is essential to find new materials to host ILEs for realizing high t_{Li^+} and fast Li^+ conduction.

Hydrogen-bonded organic framework (HOF) is another kind of porous framework material. Compared with the competitors (MOFs and COFs) with strong chemical bonds, *i.e.*, coordination bond or covalent bond, HOFs are constructed by weak non-covalent interactions [26, 27]. This makes it easier for HOF to accommodate guest molecules and realize the uniform distribution. In addition, the continuous hydrogen bond networks with abundant electronegative transfer sites are favorable for Li^+ transport [28, 29]. These advantages make HOF a promising candidate as ILEs host for Li^+ conductors [30, 31].

Herein, the fabrication of a hydrogen-bonded organic framework-ionic liquid composite quasi-solid electrolyte (CQSE) was reported. Specifically, HOF lamellar framework was prepared by self-stacking of HOF nanosheets, followed by high temperature treatment (HT, 120 °C drying) and then soaking in diluted ILE (DILE) with acetonitrile to fabricate HT-HOF-IL CQSE. The physicochemical structure and Li^+ transfer performance of HT-HOF-IL CQSE were systematically investigated. We demonstrate that, the weak non-covalent interaction within HOF, *i.e.*, hydrogen bond interaction, together with the interaction between ILE and HOF, co-contribute to the access and uniform distribution of ILE in HOF lamellar framework. The HOF lamellar framework can inhibit the ion migration of ILE through generated interactions, which then serves as additional Li^+ transfer sites. As a result, HT-HOF-IL CQSE achieves high ionic conductivities of 5.8×10^{-4} and 5.7×10^{-5} S·cm^{-1} at −20 and −60 °C, respectively. Meanwhile, the t_{Li^+} of HT-HOF-IL CQSE reaches 0.69. These comprehensive performances are superior to most reported IL-based electrolytes. Furthermore, the assembled $LiFePO_4$ (LFP)|Li cells exhibit excellent cycling performances from −20 to 60 °C. This work may pave a new avenue for the development of high-performance IL-based composite electrolytes.

2 Experimental

2.1 Materials and chemicals

1,2,4,5-Tetrakis (4-carboxyphenyl)-benzene (H4TCPB, 98.33%) was purchased from Jilin Chinese Academy of Sciences-Yanshen Technology Co., Ltd. 1-Ethyl-3-methylimidazolium bis(trifluoromethylsulfonyl) imide ([EMIM]TFSI, 97%), N,N-dimethylformamide (DMF, analytical reagent (AR), 99.5%), acetonitrile (C_2H_3N, AR, 99.5%), lithium bis(trifluoromethane) sulfonamide (LiTFSI, 99.9%) and N-methyl-2-pyrrolidone (NMP, 99.5%) were purchased from Macklin Reagent. Lithium iron phosphate (LFP), carbon black (super P) and polyvinylidene fluoride (PVDF, M_W = 1,100,000) were provided by Guangdong Canrd New Energy Technology Co., Ltd. Ultrapurified water was utilized throughout the experiment.

2.2 Preparation of HOF lamellar framework and HT-HOF-IL CQSE

H4TCPB (55.8 mg, 0.1 mmol) was dissolved into DMF (7.5 mL) to obtain a clear solution by ultrasound for 10 min. Then, the uniform colloidal suspension of HOF-H4TCPB nanosheets was obtained by adding 175 mL water into the above solution and stirring in water bath at 30 °C for 2 h. ILE was prepared by stirring and mixing LiTFSI and IL in a molar ratio of 1:4 at room temperature. Meanwhile, solid LiTFSI, IL and acetonitrile were mixed in a molar ratio of 1:4:10 to prepare the DILE under argon atmosphere.

70 mL deionized water was added to 30 mL above colloidal suspension and stirred at room temperature for 30 min. Then vacuum filtering the above diluted HOF nanosheets solution on a nylon support and dried at 30 °C for 6 h to obtain the free-standing HOF lamellar framework. Then the HOF lamellar framewrok was heated at 120 °C for 6 h to obtain the HT-HOF lamellar framewrok. Finally, the HT-HOF lamellar framework was soaked in the diluted ILE for 48 h under argon atmosphere and then dried at 60 °C for 24 h to obtain the HT-HOF-IL CQSE. And all samples were kept in the argon-filled glove-box.

2.3 Characterization

The morphologies of HOF nanosheets and membranes were observed by atomic force microscopy (AFM, Bruker Dimension FastScan) and scanning electron microscopy (SEM, JSM-7500F). High-resolution transmission electron microscopy (TEM, FEI Talos F200S) was employed to observe the morphology and lattice fringes of HOF nanosheets and HT-HOF-IL CQSE. X-ray diffraction (XRD, Bruker D8 Advance ECO) model was used to analyze the crystal structures of HOF nanosheets and HT-HOF-IL CQSE. The thermogravimetric analysis (TGA) of samples was texted using TGA-50 SHIMADZU from 25 to 800 °C with a heating rate of 10 °C·min^{-1} under N_2 atmosphere. The thermodynamic properties of HOF lamellar framework, HT-HOF-IL CQSE and ILEs were determined by differential scanning calorimetry (DSC, 200 F3 NETZSCH) under N_2 atmosphere. Fourier transform infrared (FTIR) spectra of HT-HOF lamellar framework, HT-HOF-IL CQSE and ILEs were obtained (400–4000 cm^{-1}) with a Nicolet MAGNA-IR560 instrument. Chemical composition and structural information of samples were elucidated by X-ray photoelectron spectroscopy (XPS, AXIS Supra, Kratos, UK). The chemical structures of HT-HOF-IL CQSE, ILEs and HOF lamellar framework were analyzed by ^{1}H NMR (Bruker 400M) through dissolving them in dimethyl sulfoxide-d6.

2.4 Electrochemical measurement

The electrolyte samples were sandwiched between two stainless sheets in CR2032 coin cells. Electrochemical impedance spectroscopy (EIS) was carried on an electrochemical station (CHI660E, Shanghai) at −60 to 40 °C. The ionic conductivities (σ) were calculated by the following equation

$$\sigma = \frac{L}{AR} \times 1000 \quad (1)$$

where R, A and L are electrolyte impedance (Ω), area (cm^2) and thickness (μm) of electrolyte, respectively.

The activation energy (E_a) of HT-HOF-IL CQSE and ILEs were calculated using Arrhenius equation

$$\sigma = A' \exp(-\frac{E_a}{R'T}) \quad (2)$$

where E_a is activation energy for ion transfer ($J \cdot mol^{-1}$), A' is pre-exponential factor, R' is gas constant ($J \cdot mol^{-1} \cdot K^{-1}$), T is temperature (K).

The t_{Li^+} was examined via direct current (DC) polarization and alternating current (AC) impedance with a Li symmetric cell and the t_{Li^+} were calculated using the following equation

$$t_{Li^+} = \frac{I_s(\Delta V - I_0 R_0)}{I_0(\Delta V - I_s R_s)} \quad (3)$$

where the value of applied voltage (ΔV) is 10 mV, I_0 and I_s are the initial current and steady current during DC polarization process, respectively, R_0 and R_s are the resistance values of electrolyte before and after DC polarization.

2.5 Electrochemical measurement

The cathode slurry was obtained by stirring LFP powder, super P and PVDF with a mass ratio of 8:1:1 in NMP solvent, then coated the resultant slurry onto Al foil and dried in vacuum at110 °C for 12 h, the areal capacity was ~ 1.8 $mAh \cdot cm^{-2}$. The preparation of $LiNi_{0.8}Co_{0.1}Mn_{0.1}O_2$ (NCM811) also followed a similar procedure, the areal capacity was ~ 2.1 $mAh \cdot cm^{-2}$. The batteries were assembled into CR2032 coin cells using LFP and NCM811 as cathode, HT-HOF-IL CQSE and polypropylene (PP, ~ 25 μm thickness, filled with ILEs) as separator and Li foil as anode, the whole cells assembly process should be conducted in argon-filled glovebox. All electrochemical measurements were tested on the LAND CT2001A measurement system.

3 Results and discussion

The preparation process of HT-HOF-IL CQSE is schematically illustrated in Fig. 1(a). Firstly, the HOF nanosheets were prepared via one-step self-assembly of H4TCPB in the mixed solution of water and DMF with molar ratio of 90:1. AFM and SEM images show that HOF nanosheets possess lateral size of ~ 1–2 μm and thickness of ~ 2 nm (Fig. 1(b) and Fig. S1 in the Electronic Supplementary Material (ESM)). TEM image (Fig. 1(c)) shows that HOF nanosheets display obvious porous structure and clear lattice fringes with (112) and (010) crystal planes and the spacing between adjacent fringes matches well with the XRD patterns (Fig. 1(d)). Then, the HOF lamellar framework was obtained by vacuum filtrating the HOF nanosheets on nylon support and drying at 30 °C for 6 h. SEM images in Fig. S2 in the ESM show that the HOF lamellar framework possesses lamellar structure with a thickness of ~ 23 μm and the XRD shows a strong diffraction peak at $2\theta = 7.18°$, corresponding to an interlayer distance of 1.23 nm (Fig. 1(d)). After

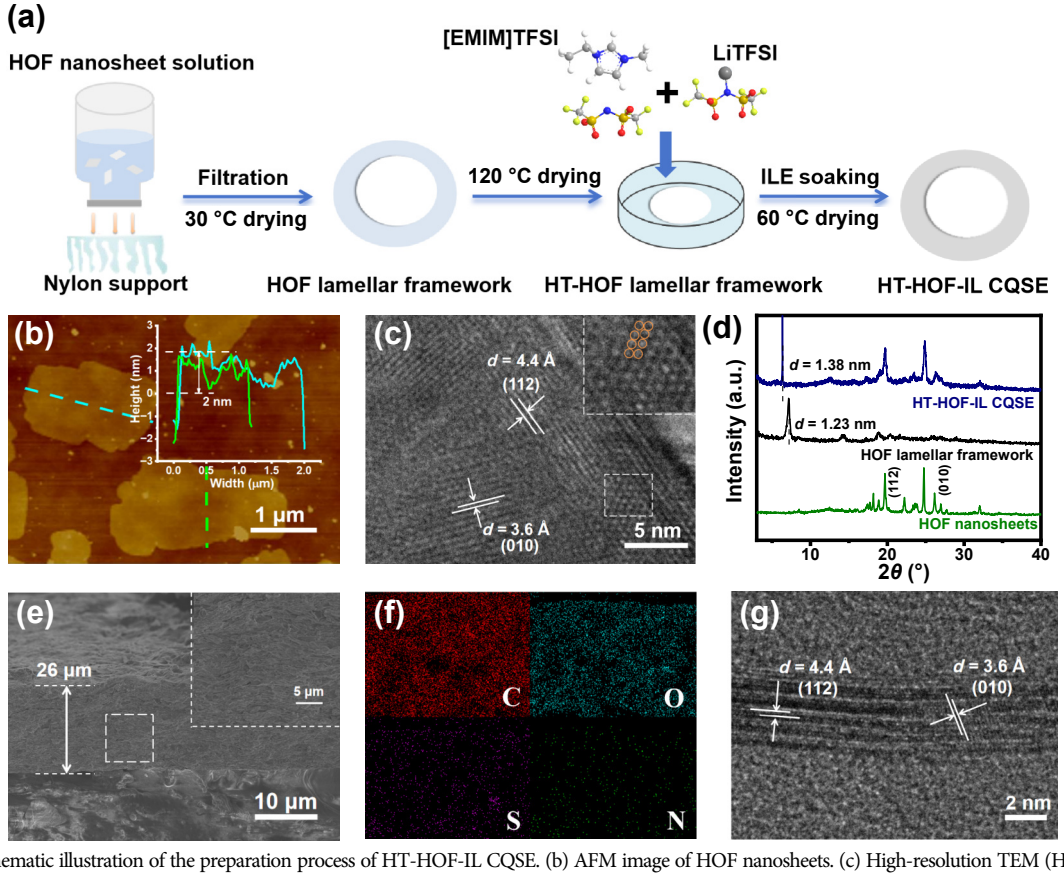

Figure 1 (a) Schematic illustration of the preparation process of HT-HOF-IL CQSE. (b) AFM image of HOF nanosheets. (c) High-resolution TEM (HRTEM) image of HOF nanosheets. (d) XRD patterns of HOF nanosheets, HOF lamellar framework and HT-HOF-IL CQSE. (e) Cross-sectional SEM image of HT-HOF-IL CQSE and (f) the corresponding EDS elemental mappings (C, O, S and N). (g) HRTEM image of HT-HOF-IL CQSE.

treating at 120 °C for 6 h, the lamellar structure becomes vague and the thickness reduces to ~ 20 μm for HT-HOF lamellar framework (Fig. S3 in the ESM), because of the loss of free water and bound water. Then, HT-HOF-IL CQSE was attained by soaking the HT-HOF lamellar framework in diluted ILEs. Here, ILE with an optimized molar ratio of LiTFSI to IL (1:4) is selected, which shows superior conduction ability and favorable affinity with HT-HOF lamellar framework (contact angle = 40°, Figs. S4 and S5 in the ESM). After the impregnation of ILE, the thickness of HT-HOF-IL CQSE re-increases to ~ 26 μm (Fig. 1(e) and Fig. S6 in the ESM), with the interlayer distance increasing to 1.38 nm (Fig. 1(d)). The corresponding energy dispersive spectroscopy (EDS) elemental mappings display that C, O, S and N elements are uniformly distributed (Fig. 1(f)), hinting the presence and uniform distribution of ILEs in HT-HOF-IL CQSE. It is worth noting that, compared with the HT-HOF lamellar framework (Fig. S7 in the ESM), HT-HOF-IL CQSE displays more obvious crystalline texture (Fig. S8 in the ESM). Meanwhile, HT-HOF-IL CQSE possesses stronger peak intensity for (112) and (010) crystal planes, where those for HOF lamellar framework can hardly be detected (Fig. 1(d)). TEM image of HT-HOF-IL CQSE also shows obvious (112) and (010) crystal planes (Fig. 1(g)). These suggest that the addition of ILE does not obviously destroy the crystalline structure of HOF and the ILE may regularly distribute in HT-HOF-IL CQSE.

The topological structure of HOF nanosheet is illustrated in Fig. 2(a), each H4TCPB connects with four surrounding H4TCPB through hydrogen bonds (–COOH···H_2O), generating a two-dimensional (2D) molecule layer along the ab plane. These 2D layers stack along the *c*-axis direction via π–π interaction, forming three-dimensional (3D) porous HOF lamellar framework. To detect the influence of heat treatment and ILE impregnation on the crystal structure of HOF nanosheets, the HOF nanosheets were heated at 120 °C for 6 h, followed by mixing with diluted ILE (HT-HOF+ILE) and the XRD was conducted. Figure 2(b) shows that the crystalline structure of HOF nanosheet is not destroyed after the heat treatment and ILE impregnation. Note that the peaks for (112) and (010) crystal planes of HOF nanosheets shift to higher angles for HT-HOF+ILE, which means the shrinkage of unit cell [32]. To explore the reason for above changes, some more characterizations were conducted. TGA results are shown in Fig. 2(c), the weight loss from 85 to 120 °C is ascribed to the loss of free water and bound water, which indicates that water molecules participate in the formation of hydrogen bond (–COOH···H_2O) and assist the fabrication of HOF nanosheets [33]. The ILE content in HT-HOF-IL CQSE was calculated to be ~ 19.2 wt.% based on TGA results. In comparison, no obvious water loss is observed during this temperature range for HT-HOF-IL CQSE, because of the heat treatment process at 120 °C. DSC results verify the above findings, as shown in Fig. 2(d), HOF lamellar framework displays melting peaks at 0 and 5 °C, corresponding to the free water and bound water, respectively. Similarly, there is no melting peak of water for HT-HOF-IL CQSE.

Besides, a crystallizing peak appears at ~ −24.8 °C for ILE and the corresponding crystallization peak of HT-HOF-IL CQSE moves to a higher temperature (−15.4 °C), which may be related to the generated new interactions between ILE and HT-HOF nanosheets [34]. Furthermore, the XPS O 1s spectra of samples were performed, in which the O 1s spectra of HT-HOF lamellar framework can be deconvoluted into C–O and C=O bonds at 533.15 and 531.62 eV, respectively. After the HT-HOF lamellar framework is impregnated with ILE, the peak for C=O occurs blue shift of ~ 0.6 eV (Fig. 2(e)). Meanwhile, Fig. 2(f) shows that, compared to HT-HOF lamellar framework (1.46 nm), the average pore size of HT-HOF-IL CQSE slightly reduces to 1.39 nm, which may be attributed to the shrinkage of unit cell and the presence of ILE in the pore of HT-HOF nanosheets.

To further detect the interactions between ILE and HT-HOF lamellar framework, FTIR (Fig. 3(a)) was conducted. The peaks at

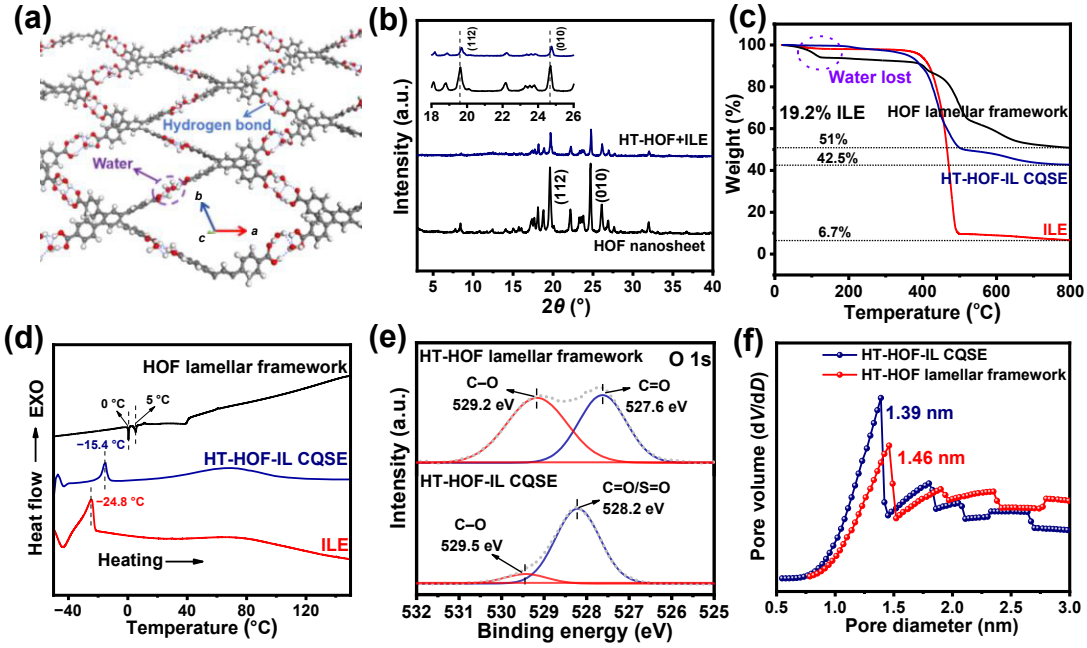

Figure 2 (a) Schematic topological structure of HOF nanosheet. (b) XRD patterns of HOF nanosheet and HT-HOF+ILE (the mixture of HT-HOF nanosheets and ILE). (c) TGA curves of ILE, HOF lamellar framework and HT-HOF-IL CQSE. (d) DSC curves of HOF lamellar framework, HT-HOF-IL CQSE and ILE. EXO stands for exothermic. (e) XPS O 1s spectra of HT-HOF lamellar framework and HT-HOF-IL CQSE. (f) Pore size distribution of HT-HOF lamellar framework and HT-HOF-IL CQSE.

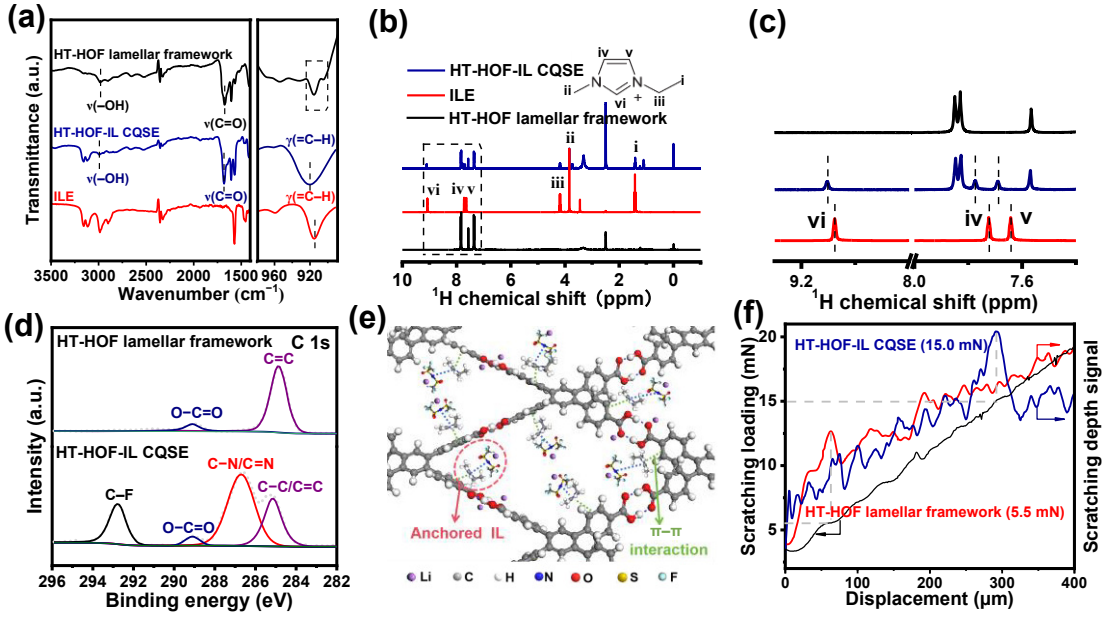

Figure 3 (a) FTIR spectra of ILE, HT-HOF lamellar framework and HT-HOF-IL CQSE. (b) and (c) ^{1}H NMR spectra of ILE, HT-HOF lamellar framework and HT-HOF-IL CQSE. (d) XPS C 1s spectra of HT-HOF lamellar framework and HT-HOF-IL CQSE. (e) Schematic ILE distribution in HT-HOF-IL CQSE (the π–π interactions between $[EMIM]^+$ and HT-HOF nanosheet are highlighted in green dash lines). (f) Nanoscratch measurement of HT-HOF lamellar framework and HT-HOF-IL CQSE.

2979 and 1670 cm^{-1} are attributed to –OH and C=O stretching vibration. It is worth noting that the characteristic peaks of HT-HOF-IL CQSE appear blue shift (2992 and 1680 cm^{-1}), which further verifies the enhancement of hydrogen bond [35]. Meanwhile, the characteristic peak of carboxyl dimer appears for HT-HOF lamellar framework at 917 cm^{-1}. Together with the TGA and DSC results, these demonstrate the removal of bound water between H4TCPB (Fig. S9 in the ESM). Additionally, the wide absorption band at 914 cm^{-1} is assigned to the =C–H out-of-plane bending vibration of imidazole ring. The blue shift of =C–H (920 cm^{-1}) for HT-HOF-IL CQSE indicates that there may be interaction between $[EMIM]^+$ and HT-HOF lamellar framework [36, 37]. Then, ^{1}H NMR was performed to detect the interactions. Figures 3(b) and 3(c) reveal that all the imidazolium protons of HT-HOF-IL CQSE shift downfield as compared with ILE, confirming that there are interactions between HT-HOF lamellar framework and $[EMIM]^+$ cations. These interactions should result from the generated π–π interaction between $[EMIM]^+$ and HT-HOF nanosheets. This view can be further proved by XPS C 1s and ^{13}C NMR results. As shown in Fig. 3(d), the shift of C=C peak for HT-HOF-IL CQSE is attributed to the generated π–π interactions between $[EMIM]^+$ and HT-HOF lamellar framework [38]. Similarly, the shift of carbon on benzene ring also proves this point (Fig. S10 in the ESM). Accordingly, the distribution of ILEs in HT-HOF-IL CQSE is supposed in Fig. 3(e), the $[EMIM]^+$ generates π–π interactions with HT-HOF nanosheets and the negatively charged pore could capture Li^+ and electrostatically repulse the free $TFSI^-$. The TEM and corresponding EDS elemental mappings of HT-HOF-IL CQSE after ultrasonic in acetonitrile display the stable existence of ILEs, testifying the interactions between $[EMIM]^+$ and HT-HOF lamellar framework (Fig. S11 in the ESM). The suppositional π–π interactions were further verified by nanoscratch measurement. Figure 3(f) shows that HT-HOF-IL CQSE possesses a critical loading of 15.0 mN, ~ 3 times of that of HT-HOF lamellar framework (5.5 mN), which confirms the enhancement of interlayer interaction. Collectively, these results demonstrate that the weak hydrogen bonding interactions within HOF nanosheets, together with the generated interactions between ILE and HOF, enable the access and uniform distribution of ILE in HOF lamellar framework.

The uniform distribution of ILE in HT-HOF-IL CQSE then confers efficient Li^+ transport property, especially at low temperatures (< 0 °C). The ionic conduction performance of HT-HOF-IL CQSE at the temperature range of −60 to 40 °C is shown in Fig. 4(a) and Figs. S12 and S13 in the ESM. HT-HOF-IL CQSE shows a high ionic conductivity of 1.4×10^{-3} $S \cdot cm^{-1}$ at 40 °C, surpassing most polymer-based electrolytes and ionogel electrolytes (Fig. 4(f)) and even close to ILE. Notably, even at −60 °C, the ionic conductivity of HT-HOF-IL CQSE reaches 5.7×10^{-5} $S \cdot cm^{-1}$. In contrast, ILE shows a significant decline in ionic conductivity at low temperature, exhibiting poor ionic conductivity at −60 °C (1.9×10^{-6} $S \cdot cm^{-1}$). Such obvious improvement of low-temperature ionic conductivity for HT-HOF-IL CQSE should be ascribed to that the nanoscale pores could effectively alleviate the ion aggregation of ILE and the uniformly distributed ILE in the pores could serve as the continuous and stable transfer pathways, affording rapid Li^+ transport even at low temperatures (Fig. 4(c)). For ILE and PP separator, the conductivity suffers from obvious deterioration at low temperatures due to the sharply increased viscosity. Additionally, the inherent electronegative transfer sites (*i.e.*, $-COO^-$) on HOF nanosheets could also serve as transfer sites at low temperatures, which originate from the partially deprotonated HOF framework during the socking process [39]. This can be confirmed by the conductivity-temperature relationship of HT-HOF-IL CQSE. The conductivity–temperature relationship of HT-HOF-IL CQSE follows Arrhenius-type behavior, showing a low fitted E_a of 0.19 eV. This demonstrates the temperature-stable distribution of ILE within HT-HOF-IL CQSE. In comparison, ILE shows an obviously increased E_a from 0.21 eV at −60–−20 °C to 0.45 eV at −20–40 °C, owing to the increased viscosity of bulk ILE with the decrease of temperature.

Then, the t_{Li^+} of electrolytes at 30 °C were tested through

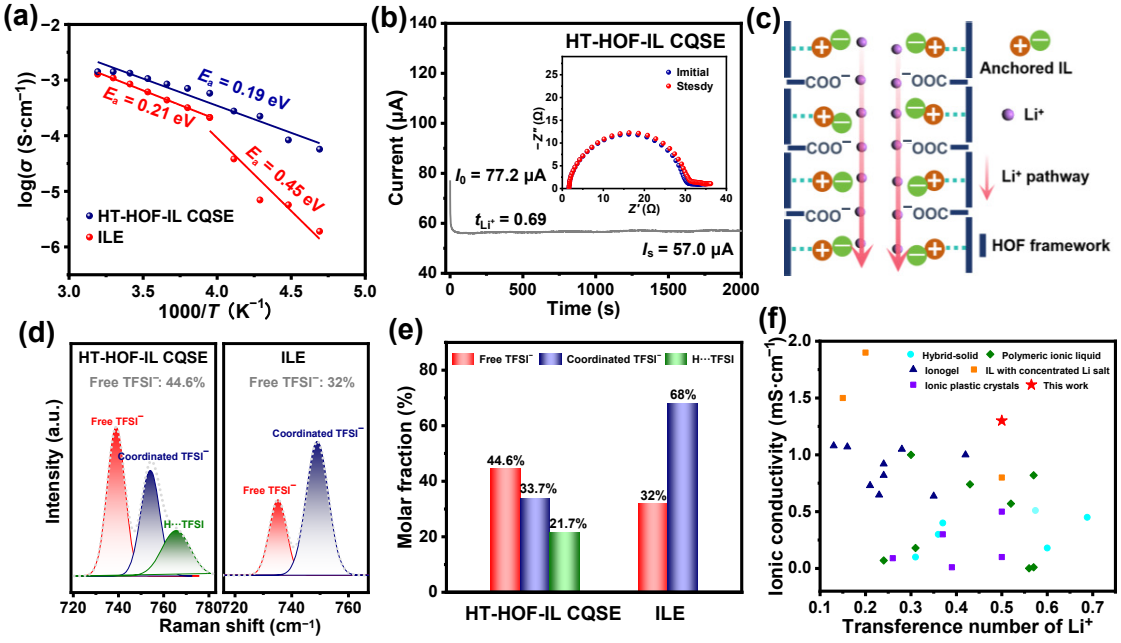

Figure 4 (a) Temperature-dependent conductivities of HT-HOF-IL CQSE and ILE. (b) Chronoamperometry profile of symmetric Li|HT-HOF-IL CQSE|Li cell with applied potential of 10 mV at 30 °C and AC impedance spectra before and after polarization (inset). (c) Schematic diagram of Li^+ transfer pathway in HT-HOF-IL CQSE. (d) Raman spectra of HT-HOF-IL CQSE and ILE. (e) The molar fraction of different coordination states of $TFSI^-$ in HT-HOF-IL CQSE and ILE. (f) Comparison of ionic conductivity and transference number of ionic liquid based electrolytes.

Bruce–Vincent–Evans (BVE) method (Fig. 4(b) and Fig. S14 in the ESM). HT-HOF-IL CQSE shows a high t_{Li^+} of 0.69, higher than most polymer-based electrolytes and ionogel electrolytes (Fig. 4(f) and Table S1 in the ESM). In addition, the t_{Li^+} of HT-HOF-IL CQSE and ILE at −20 °C were also measured. As shown in Fig. S15 in the ESM, HT-HOF-IL CQSE also shows a high t_{Li^+} value of 0.60. The high t_{Li^+} of HT-HOF-IL CQSE should be attributed to that, the presence of HOF lamellar framework can effectively alleviate the ion aggregation and inhibits the ion migration of ILE, thus realizing selective and rapid transfer of Li^+. As shown in Figs. 4(d) and 4(e), HT-HOF-IL CQSE displays 44.6% of uncoordinated $TFSI^-$, while ILE shows a free $TFSI^-$ anion intensity of only 32%. These demonstrate the more proportion of free Li^+ in HT-HOF-IL CQSE. Then, the migration of $TFSI^-$ could be effectively hampered by the generated hydrogen bonding interactions between $TFSI^-$ and –COOH in HOF lamellar framework, which can be verified by the shift of $-CF_3$ on $TFSI^-$ (Fig. S16 in the ESM). As a result, increased t_{Li^+} is obtained. In addition, the new peak at 765 cm^{-1} is assigned to the formation of HTFSI, which should be ascribed to the combination of H^+ from HOF framework and $TFSI^-$. XPS N 1s spectra of HOF-IL CQSE (Fig. S17 in the ESM) can further prove the existence of HTFSI [40, 41]. Thus, the partially deprotonated HOF framework forms more electronegative sites (*i.e.*, $-COO^-$) for Li^+ transfer (Fig. 4(c)). By contrast, ILE and PP separator display low t_{Li^+} at 30 °C (0.33) and −20 °C (0.19), as PP separator is not conducive to the dissociation of ILE [42].

To evaluate the application possibility of HT-HOF-IL CQSE and ILE at low temperatures, the galvanostatic cycling curves of Li symmetrical cells were tested at 0.2 mA·cm^{-2} and −20 °C. Figure 5(a) displays that ILE has an overpotential of ~ 90 mV at 0.2 mA·cm^{-2} and −20 °C and suffers from short-circuit within 1100 h. In comparison, Li|HT-HOF-IL CQSE|Li symmetric cell could stably cycle for more than 1500 h with a low overpotential of 40 mV. Such performance should result from the high conduction property of HT-HOF-IL CQSE at low temperatures. The Li^+ deposition behavior was detected by SEM (Figs. S18 and S19 in the ESM) and there were obvious irregular lithium dendrites on the lithium electrode surface of cycled Li|ILE|Li cell. In comparison, the lithium electrode surface of Li|HT-HOF-IL CQSE|Li cell remains uniform and smooth after cycling. The surface composition of Li anode of cycled Li|HT-HOF-IL CQSE|Li and Li|ILE|Li was detected by XPS. As shown in Fig. S20 in the ESM, there is almost no solid electrolyte interface (SEI) formed on the surface of Li anode of cycled Li|ILE|Li. In comparison, for Li|HT-HOF-IL CQSE|Li, rich SEI in the form of LiF, Li_3N and Li_2S is detected on the Li anode surface. This SEI layer may effectively prevent the corrosion of Li anode in the subsequent cycling process and improve the cycling stability of battery [43].

Then, HT-HOF-IL CQSE was assembled into LFP|Li cells to evaluate the cycling and rate performances at low temperatures. Figure 5(b) shows that the discharge capacity of LFP|HT-HOF-IL CQSE|Li reaches 61.1 mAh·g^{-1} at −20 °C under 0.5 C and there is almost no capacity decay. In comparison, LFP|ILE|Li suffers from a sharp decline in discharge capacity from 54.9 to 36.1 mAh·g^{-1} after 112 cycles. This should be ascribed to that, the viscosity of ILE increases at low temperatures, which hinders the transfer of Li^+. Moreover, the galvanostatic charge/discharge curves show that LFP|HT-HOF-IL CQSE|Li cell exhibits a low polarization voltage of 0.22 V. The voltage plateaus remain basically the same within 300 cycles, which indicates that the HT-HOF-IL CQSE has a stable charging and discharging performance (Fig. 5(c)). Rate capability is an essential index of electrochemical performance. Figure 5(d) reveals the rate capability of HT-HOF-IL CQSE and ILE at −20 °C, the discharge capacity of LFP|ILE|Li suffers from dramatic reduction at 0.6 C and drops to 0 at 0.8 C, which should originate from the low t_{Li^+} due to the increased viscosity of ILE at low temperatures. While LFP|HT-HOF-IL CQSE|Li maintains excellent cycling performance at each current rate from 0.2 to 2 C. After

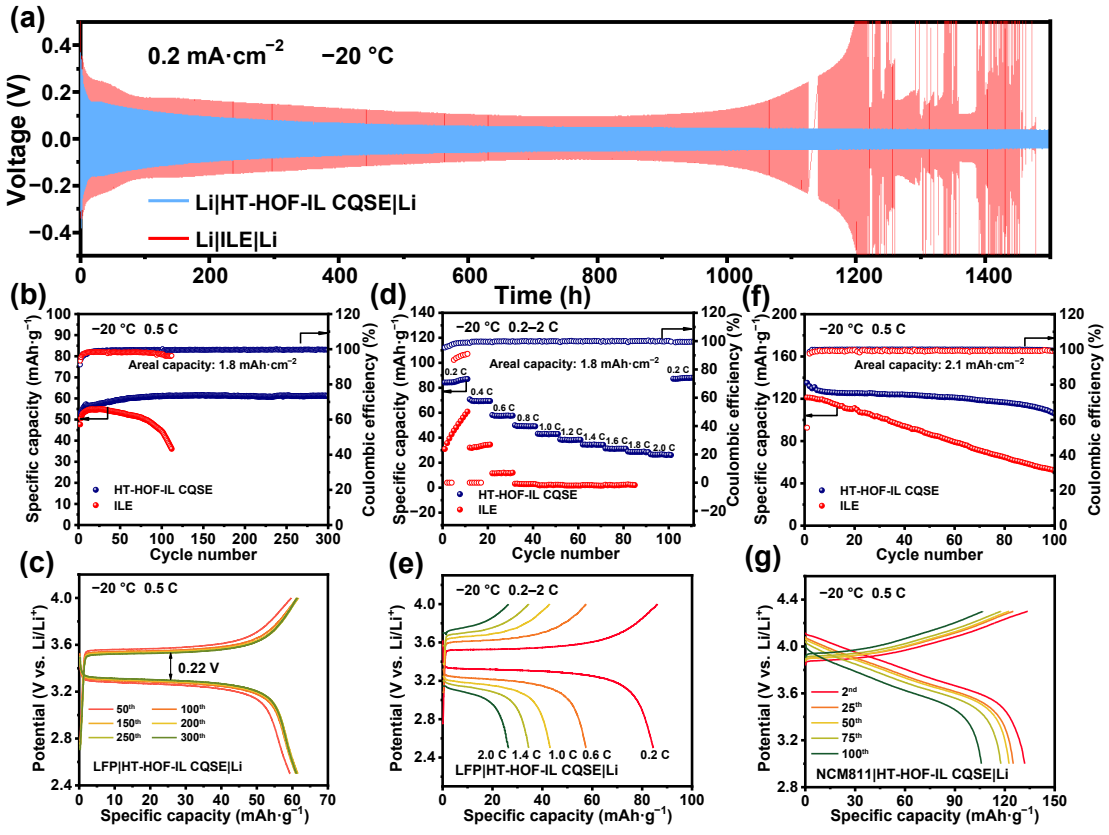

Figure 5 (a) Long-term cycling of Li|HT-HOF-IL|Li and Li|ILE|Li symmetrical cells at −20 °C. (b) Cycling performance of LFP|HT-HOF-IL CQSE|Li and LFP|ILE|Li cells at 0.5 C under −20 °C. (c) The charge–discharge profiles of LFP|HT-HOF-IL CQSE|Li cell at 0.5 C and −20 °C. (d) Rate performance of LFP|HT-HOF-IL CQSE|Li and LFP|ILE|Li cells at −20 °C. (e) The charge–discharge profiles of LFP|HT-HOF-IL CQSE|Li cell under various rates at −20 °C. (f) Cycling performance of NCM811|HT-HOF-IL CQSE|Li and NCM811|ILE|Li cells at 0.5 C under −20 °C. (g) The charge–discharge profiles of NCM811|HT-HOF-IL CQSE|Li cell at 0.5 C and −20 °C.

cycling at 2 C, the capacity can recover to 88.3 mAh·g^{-1}. This better cycling performance is attributed to the higher t_{Li^+}, which can effectively inhibit the concentration polarization and improve the rate performance of LFP|HT-HOF-IL CQSE|Li. Furthermore, LFP|HT-HOF-IL CQSE|Li cell displays low polarization voltage and smooth curves at different rates (Fig. 5(e)). Such superior cycling performances of LFP|HT-HOF-IL CQSE|Li cells should be attributed to the continuous and stable transfer sites in HT-HOF-IL CQSE. $LiNi_{0.8}Co_{0.1}Mn_{0.1}O_2$ (NCM811) was also selected to evaluate the cells assembled with HT-HOF-IL CQSE and ILE for high-voltage cathode. Figures 5(f) and 5(g) reveal that, at 0.5 C and −20 °C, the specific capacity of NCM811|HT-HOF-IL CQSE|Li slowly decays from 132 to 107 mAh·g^{-1} with 81% retention after 100 cycles and the average coulombic efficiency is 99.87%. In comparison, NCM811|ILE|Li suffers from dramatic reduction in discharge capacity from 121.2 to 52.3 mAh·g^{-1}.

To evaluate the application potential of HT-HOF-IL CQSE at room temperature, the cycling performance of cell assembled with HT-HOF-IL CQSE was also tested at 25 °C. As shown in Fig. S21 in the ESM, an initial discharge capacity of 144.5 mAh·g^{-1} is observed, which slightly decreases to 128.5 mAh·g^{-1} after 300 cycles (0.03% per cycle). And the half-cell exhibits low polarization voltage. Figure S22 in the ESM shows the rate performance of HT-HOF-IL CQSE. Similarly, LFP|HT-HOF-IL CQSE|Li shows excellent rate performance from 0.2–3 C at room temperature. In addition, the cycling performance of LFP|HT-HOF-IL CQSE|Li at 60 °C was also tested. Figure S23 in the ESM shows that LFP|HT-HOF-IL CQSE|Li can operate at 0.5 C and 60 °C for more than 300 cycles and there is almost no capacity decay. Collectively, these demonstrate the great potential of HT-HOF-IL CQSE as electrolyte for high-performance lithium batteries, especially at low temperatures.

4 Conclusion

In summary, an IL-based composite quasi-solid electrolyte was prepared by confining ILEs into the pore of HOF lamellar framework. We demonstrate that the weak hydrogen bonding interactions within HOF nanosheets, together with the generated interactions between ILE and HOF, enable uniform and continuous distribution of ILE in HOF lamellar framework. The uniform distribution and anchoring of ILE in the pores could serve as continuous and stable transfer pathways. Meanwhile, the inherent electronegative transfer sites (*i.e.*, $-COO^-$) originated from partially deprotonated HOF nanosheets could also serve as transfer sites. Together, these afford rapid Li^+ transport at low temperatures. HT-HOF-IL CQSE shows a high ionic conductivity of 5.7×10^{-5} S·cm^{-1} at −60 °C, as compared to 1.9×10^{-6} S·cm^{-1} of ILE. At 40 °C, HT-HOF-IL CQSE also displays excellent ionic conduction property (1.4×10^{-3} S·cm^{-1}), surpassing most polymer-based electrolytes and ionogel electrolytes and even close to ILE. More importantly, compared with PP separator, the HOF lamellar framework with nanoscale pores could inhibit the ion migration of ILE through π–π

interaction, realizing selective and rapid transfer of Li^+. Therefore, HT-HOF-IL CQSE exhibits a high t_{Li^+} of 0.69, two times of that of ILE (0.33). The assembled Li symmetrical cell can operate at 0.2 mA·cm^{-2} at −20 °C for more than 1500 h and no obvious polarization is observed. The assembled $LiFePO_4$|HT-HOF-IL CQSE|Li cell exhibits excellent cycling and rate performance over a wide temperature range (−20–60 °C). Our work may expand the application of IL-based electrolytes in solid-state lithium batteries and provide insight into the unique interactions within HOF.

Electronic Supplementary Material: Supplementary material (SEM and TEM images, XPS spectra, AC impedance spectra before and after polarization and chronoamperometry profiles, cycling performance *etc.*) is available in the online version of this article at https://doi.org/10.26599/NR.2025.94906993.

Data availability

All data needed to support the conclusions in the paper are presented in the manuscript and the Electronic Supplementary Material. Additional data related to this paper may be requested from the corresponding author upon request.

Acknowledgements

The authors would like to acknowledge the financial support from National Key R&D Program of China (No. 2022YFB3805204), Joint Foundation for Science and Technology Research & Development Plan of Henan Province (Nos. 222301420003 and 232301420038), China Postdoctoral Science Foundation (No. 2022TQ0293) and Key Science and Technology Project of Henan Province (No. 221100240200-06). Center of Advanced Analysis & Gene Sequencing, Zhengzhou University is also highly acknowledged.

Declaration of competing interest

The authors declare that they have no known competing financial interests or personal relationships that could have appeared to influence the work reported in this paper.

Author contribution statement

J. M. Z.: Investigation, data curation, writing – original draft. Y. T. W.: Methodology, formal analysis. C. Y. W.: Formal analysis, conceptualization. Y. L.: Supervision, resources. Z. R. Y.: Software, validation. S. Y. Z.: Investigation, formal analysis. W. P. L.: Project administration. W. J. W.: Supervision, writing – review & editing. J. T. W.: Resources, methodology, funding acquisition. All the authors have approved the final manuscript.

Use of AI statement

None.

References

[1] Yang, Q. W.; Zhang, Z. Q.; Sun, X. G.; Hu, Y. S.; Xing, H. B.; Dai, S. Ionic liquids and derived materials for lithium and sodium batteries. *Chem. Soc. Rev.* **2018**, *47*, 2020–2064.

[2] Fan, L.; Xie, H. B.; Hu, Y. Y.; Caixiang, Z. M.; Rao, A. M.; Zhou, J.; Lu, B. G. A tailored electrolyte for safe and durable potassium ion batteries. *Energy Environ. Sci.* **2023**, *16*, 305–315.

[3] Huang, Z. J.; Lai, J. C.; Kong, X.; Rajkovic, I.; Xiao, X.; Celik, H.; Yan, H. P.; Gong, H. X.; Rudnicki, P. E.; Lin, Y. J. et al. A solvent-anchored non-flammable electrolyte. *Matter* **2023**, *6*, 445–459.

[4] Zhu, G. R.; Zhang, Q.; Liu, Q. S.; Bai, Q. Y.; Quan, Y. Z.; Gao, Y.; Wu, G.; Wang, Y. Z. Non-flammable solvent-free liquid polymer electrolyte for lithium metal batteries. *Nat. Commun.* **2023**, *14*, 4617.

[5] Giffin, G. A. Ionic liquid-based electrolytes for "beyond lithium" battery technologies. *J. Mater. Chem. A* **2016**, *4*, 13378–13389.

[6] Wang, Z. C.; Zhang, F. R.; Sun, Y. Y.; Zheng, L.; Shen, Y. B.; Fu, D. S.; Li, W. F.; Pan, A. R.; Wang, L.; Xu, J. J. et al. Intrinsically nonflammable ionic liquid-based localized highly concentrated electrolytes enable high-performance Li-metal batteries. *Adv. Energy Mater.* **2021**, *11*, 2003752.

[7] Sun, H.; Zhu, G. Z.; Zhu, Y. M.; Lin, M. C.; Chen, H.; Li, Y. Y.; Hung, W. H.; Zhou, B.; Wang, X.; Bai, Y. X. et al. High-safety and high-energy-density lithium metal batteries in a novel ionic-liquid electrolyte. *Adv. Mater.* **2020**, *32*, 2001741.

[8] Zheng, Y. Y.; Wang, D.; Kaushik, S.; Zhang, S. N.; Wada, T.; Hwang, J.; Matsumoto, K.; Hagiwara, R. Ionic liquid electrolytes for next-generation electrochemical energy devices. *EnergyChem* **2022**, *4*, 100075.

[9] Tang, X.; Lv, S. Y.; Jiang, K.; Zhou, G. H.; Liu, X. M. Recent development of ionic liquid-based electrolytes in lithium-ion batteries. *J. Power Sources* **2022**, *542*, 231792.

[10] Borodin, O.; Self, J.; Persson, K. A.; Wang, C. S.; Xu, K. Uncharted waters: Super-concentrated electrolytes. *Joule* **2020**, *4*, 69–100.

[11] Yao, Z. C.; Zhao, S. S.; Yang, S. N.; Ma, W. T.; Gong, J. J.; Rong, J. F.; Hou, G. L.; Chen S. M. Multifunctional polyzwitterion ionic liquid based solid-state electrolytes for enhancing the low-temperature performance of lithium-metal batteries. *Chem. Eng. J.* **2024**, *495*, 153005.

[12] Wang, Z. C.; Zhang, H. Y.; Xu, J. J.; Pan, A. R.; Zhang, F. R.; Wang, L.; Han, R.; Hu, J. C.; Liu, M. N.; Wu, X. D. Advanced Ultralow-concentration electrolyte for wide-temperature and high-voltage Li-metal batteries. *Adv. Funct. Mater.* **2022**, *32*, 2112598.

[13] Zhang, H. Q.; Qu, W. J.; Chen, N.; Huang, Y. X.; Li, L.; Wu, F.; Chen, R. J. Ionic liquid electrolyte with highly concentrated LiTFSI for lithium metal batteries. *Electrochim. Acta* **2018**, *285*, 78–85.

[14] Nordness, O.; Brennecke, J. F. Ion dissociation in ionic liquids and ionic liquid solutions. *Chem. Rev.* **2020**, *120*, 12873–12902.

[15] Lee, S.; Park, K.; Koo, B.; Park, C.; Jang, M.; Lee, H.; Lee, H. Safe, stable cycling of lithium metal batteries with low-viscosity, fire-retardant locally concentrated ionic liquid electrolytes. *Adv. Funct. Mater.* **2020**, *30*, 2003132.

[16] Watanabe, M.; Thomas, M. L.; Zhang, S. G.; Ueno, K.; Yasuda, T.; Dokko, K. Application of ionic liquids to energy storage and conversion materials and devices. *Chem. Rev.* **2017**, *117*, 7190–7239.

[17] Liu, X.; Mariani, A.; Diemant, T.; Dong, X.; Su, P. H.; Passerini, S. Locally concentrated ionic liquid electrolytes enabling low-temperature lithium metal batteries. *Angew. Chem., Int. Ed.* **2023**, *62*, e202305840.

[18] Yu, L.; Yu, L.; Liu, Q.; Meng, T.; Wang, S.; Hu, X. L. Monolithic task-specific ionogel electrolyte membrane enables high-performance solid-state lithium-metal batteries in wide temperature range. *Adv. Funct. Mater.* **2022**, *32*, 2110653.

[19] Zhou, P.; Zhang, X. K.; Xiang, Y.; Liu, K. Strategies to enhance Li^+ transference number in liquid electrolytes for better lithium batteries. *Nano Res.* **2023**, *16*, 8055–8071.

[20] Liu, X.; Mariani, A.; Diemant, T.; Di Pietro, M. E.; Dong, X.; Su, P. H.; Mele, A.; Passerini, S. PFAS-free locally concentrated ionic liquid electrolytes for lithium metal batteries. *ACS Energy Lett.* **2024**, *9*, 3049–3057.

[21] Shi, Q. X.; Guan, X.; Pei, H. J.; Chang, C.; Qu, H.; Xie, X. L.; Ye, Y. S. Functional covalent triazine frameworks-based quasi-solid-state electrolyte used to enhance lithium metal battery safety. *Batteries Supercaps* **2020**, *3*, 936–945.

[22] Tian, X. L.; Chen, S. H.; Zhang, P.; Yang, P.; Yi, Y. K.; Wang, T.; Fang, B. R.; Liu, P.; Qu, L.; Li, M. T. et al. Covalent organic frameworks with immobilized anions to liberate lithium ions: Quasi-solid electrolytes with enhanced rate capabilities. *Electrochim. Acta* **2021**, *389*, 138585.

[23] Ho, J. W.; Choi, J.; Kim, D. G.; Ha, C.; Koo, J. K.; Nam, M. G.; Kim, J.; Lee, J. H.; Kim, M.; Moon, M. W. et al. Bimetallic UiO-66(Zr/Ti)-ionic liquid grafted fillers with intensified lewis acidity for high-performance composite solid electrolytes. *Adv. Funct. Mater.* **2024**, *34*, 2308250.

[24] Wang, Z. Q.; Tan, R.; Wang, H. B.; Yang, L. Y.; Hu, J. T.; Chen, H. B.; Pan, F. A metal-organic-framework-based electrolyte with nanowetted interfaces for high-energy-density solid-state lithium battery. *Adv. Mater.* **2018**, *30*, 1704436.

[25] Liu, H. L.; Pan, H. G.; Yan, M.; Zhang, X.; Jiang, Y. Z. Extraordinary ionic conductivity excited by hierarchical ion-transport pathways in MOF-based quasi-solid electrolytes. *Adv. Mater.* **2023**, *35*, 2300888.

[26] Zhao, H. F.; Zhou, Z. W.; Feng, X. N.; Liu, C.; Wu, H.; Zhou, W.; Wang, H. L. Hydrogen-bonded organic framework for red light-mediated photocatalysis. *Nano Res.* **2023**, *16*, 8809–8816.

[27] Chen, Y.; Li, J. Y.; Zhu, Q.; Fan, K.; Cao, Y. Q.; Zhang, G. Q.; Zhang, C. Y.; Gao, Y. B.; Zou, J. C.; Zhai, T. Y. et al. Two-dimensional organic supramolecule via hydrogen bonding and π–π stacking for ultrahigh capacity and long-life aqueous zinc-organic batteries. *Angew. Chem., Int. Ed.* **2022**, *61*, e202116289.

[28] Wang, C. L. Weak intermolecular interactions for strengthening organic batteries. *Energy Environ. Mater.* **2020**, *3*, 441–452.

[29] Wu, Y. L.; Mao, X. N.; Zhang, M. C.; Zhao, X.; Xue, R. J.; Di, S. J.; Huang, W.; Wang, L.; Li, Y. Y.; Li, Y. G. 2D molecular sheets of hydrogen-bonded organic frameworks for ultrastable sodium-ion storage. *Adv. Mater.* **2021**, *33*, 2106079.

[30] Guo, C. F.; Gao, Y.; Li, S. Q.; Wang, Y. X.; Yang, X. J.; Zhi, C. W.; Zhang, H.; Zhu, Y. F.; Chen, S. Q.; Chou, S. L. et al. Chemical-stabilized aldehyde-tuned hydrogen-bonded organic frameworks for long-cycle and high-rate sodium-ion organic batteries. *Adv. Funct. Mater.* **2024**, *34*, 2314851.

[31] Han, Z. S.; Zhang, R. H.; Jiang, J. L.; Chen, Z. H.; Ni, Y. X.; Xie, W. W.; Xu, J.; Zhou, Z.; Chen, J.; Cheng, P. et al. High-efficiency lithium-ion transport in a porous coordination chain-based hydrogen-bonded framework. *J. Am. Chem. Soc.* **2023**, *145*, 10149–10158.

[32] Liu, Y. T.; Wu, H.; Li, R. L.; Wang, J. Y.; Kong, Y.; Guo, Z. Y.; Jiang, H. F.; Ren, Y. X.; Pu, Y. C.; Liang, X. et al. MOF-COF "alloy" membranes for efficient propylene/propane separation. *Adv. Mater.* **2022**, *34*, 2201423.

[33] Yang, Z. W.; Zhang, Y. F.; Wu, W. J.; Zhou, Z. F.; Gao, H. X.; Wang, J. T.; Jiang, Z. Y. Hydrogen-bonded organic framework membrane with efficient proton conduction. *J. Membr. Sci.* **2022**, *664*, 121118.

[34] Dong, M. Y.; Zhang, K. Y.; Wan, X. Y.; Wang, S. L.; Fan, S. K.; Ye, Z. Z.; Wang, Y. Q.; Yan, Y. G.; Peng, X. S. Stable two-dimensional nanoconfined ionic liquids with highly efficient ionic conductivity. *Small* **2022**, *18*, 2108026.

[35] Yang, L.; Wang, Y. S.; Wang, J. W.; Zheng, Y. P.; Ang, E. H.; Hu, Y.; Zhu, J. X. Imidazole-intercalated cobalt hydroxide enabling the Li^+ desolvation/diffusion reaction and flame retardant catalytic dynamics for lithium ion batteries. *Angew. Chem., Int. Ed.* **2024**, *63*, e202402827.

[36] Liu, M.; Zhang, S. N.; van Eck, E. R. H.; Wang, C.; Ganapathy, S.; Wagemaker, M. Improving Li-ion interfacial transport in hybrid solid electrolytes. *Nat. Nanotechnol.* **2022**, *17*, 959–967.

[37] Zeng, Q. Y.; Mukherjee, A.; Müller, P.; Rogers, R. D.; Myerson, A. S. Exploring the role of ionic liquids to tune the polymorphic outcome of organic compounds. *Chem. Sci.* **2018**, *9*, 1510–1520.

[38] Wang, Y.; Wang, W. W.; Xie, J.; Wang, C. H.; Yang, Y. W.; Lu, Y. C. Electrochemical reduction of CO_2 in ionic liquid: Mechanistic study of Li-CO_2 batteries via *in situ* ambient pressure X-ray photoelectron spectroscopy. *Nano Energy* **2021**, *83*, 105830.

[39] Yan, Y. C.; Liu, Z.; Wan, T.; Li, W. N.; Qiu, Z. P.; Chi, C. L.; Huangfu, C.; Wang, G. W.; Qi, B.; Yan, Y. G. et al. Bioinspired design of Na-ion conduction channels in covalent organic frameworks for quasi-solid-state sodium batteries. *Nat. Commun.* **2023**, *14*, 3066.

[40] Yi, M. Y.; Li, J.; Wang, M. R.; Fan, X. M.; Hong, B.; Zhang, Z. A.; Zhang, Z.; Jiang, H.; Wang, A. N.; Lai, Y. Q. Suppressing structural degradation of single crystal nickel-rich cathodes in PEO-based all-solid-state batteries: Mechanistic insight and performance. *Energy Storage Mater.* **2023**, *54*, 579–588.

[41] Zhang, Y. F.; Huang, J. J.; Liu, H.; Kou, W. J.; Dai, Y.; Dang, W.; Wu, W. J.; Wang, J. T.; Fu, Y. Z.; Jiang, Z. Y. Lamellar ionic liquid composite electrolyte for wide-temperature solid-state lithium-metal battery. *Adv. Energy Mater.* **2023**, *13*, 2300156.

[42] Kim, D.; Liu, X.; Yu, B. Z.; Mateti, S.; O'Dell, L. A.; Rong, Q. Z.; Chen, Y. Amine-functionalized boron nitride nanosheets: A new functional additive for robust, flexible ion gel electrolyte with high lithium-ion transference number. *Adv. Funct. Mater.* **2020**, *30*, 1910813.

[43] Zhang, X. X.; Su, Q. M.; Du, G. H.; Xu, B. S.; Wang, S.; Chen, Z.; Wang, L. M.; Huang, W. H.; Pang, H. Stabilizing solid-state lithium metal batteries through *in situ* generated Janus-heterarchical LiF-rich SEI in ionic liquid confined 3D MOF/polymer membranes. *Angew. Chem., Int. Ed.* **2023**, *62*, e202304947.